



Multi-hollow Surface Dielectric Barrier Discharge: Production of Gaseous Species Under Various Air Flow Rates and Relative Humidities

Richard Cimerman¹ · Karol Hensel¹

Received: 11 April 2023 / Accepted: 10 August 2023
© The Author(s) 2023

Abstract

An evaluation of the gaseous species production by the discharge, i.e., discharge chemical activity, is very important for determining its potential for practical applications. In this work, production of gaseous species by the multi-hollow surface dielectric barrier discharge generated in a perforated ceramic substrate with the air-exposed electrode is investigated under conditions of various discharge powers (1–5 W), air flow rates (0.25–2.4 L/min) and air relative humidities (0–80%). Production of ozone O₃, nitrous oxide N₂O, nitric oxide NO, nitrogen dioxide NO₂, dinitrogen pentoxide N₂O₅ and nitric acid HNO₃ is evaluated in terms of concentration (ppm), production yield (g/kWh) and production rate (mg/h). The work demonstrates a critical impact of both air flow rate and relative humidity on prevailing discharge mode (“O₃ mode” vs. “NO_x mode”) and, thus, on overall composition and concentration of produced gaseous species. For low discharge power, the discharge operates in the “O₃ mode”, when O₃, N₂O, N₂O₅ and HNO₃ are dominant gaseous products. With the increasing power, the discharge transfers into the “NO_x mode”, when N₂O and HNO₃ along with NO and NO₂ are mostly produced. In dry air, transition from “O₃ mode” to “NO_x mode” is found for the specific input energy of 1000–1100 J/L. With an increase of air relative humidity from 20 to 80%, the transition gradually decreases from approximately 600 to 450 J/L, respectively.

Keywords Nonthermal plasma · Multi-hollow surface dielectric barrier discharge · Plasma chemistry · Gaseous species · Ozone mode · Nitrogen oxides mode · Nitrogen fixation

Introduction

The nonthermal plasma (NTP), as it is very well known, can create a high-reactive environment by initiating and maintaining various chemical reactions at ambient conditions of temperature and pressure. This feature represents one of the most important benefits of the NTP in contrast to the thermal plasma. The most frequently employed NTP sources for

✉ Richard Cimerman
richard.cimerman@fmph.uniba.sk

¹ Division of Environmental Physics, Faculty of Mathematics, Physics and Informatics, Comenius University, Mlynská Dolina F2, 842 48 Bratislava, Slovakia

effective plasma chemistry are electrical discharges which have been utilised in numerous applications including surface treatment of materials [1, 2], air flow modification and control [3, 4], air and water pollution control [5, 6], bio-decontamination [7, 8], medical [9, 10] and agricultural applications [11]. Among the discharges, the dielectric barrier discharges (DBDs) have a special position due to their simplicity, scalability, and the availability of reliable, efficient, and affordable power supplies [12]. Out of them the surface dielectric barrier discharges (SDBDs) are getting an increasing attention because of their versatility, small dimensions, and possibility for electrodes encapsulation into the dielectric, what prevents their aging and damage. To optimise utilisation of the discharges in selected applications, their proper chemical characterisation (i.e., their chemical effects) must be known in detail especially under ambient conditions.

Chemical effects of NTP are in general mainly associated with high-energy electrons with energy of the order 10 eV or even higher. The electrons collide with bulk gas molecules (such as N_2 , O_2 , H_2O) leading to their dissociation and production of short-lived high-reactive species, also known as radicals (e.g., $\cdot O$, $\cdot N$, $\cdot OH$, etc.). Apart from molecular dissociation, ion formation may also occur (e.g., O^+ , O_2^+ , N^+ , N_2^+ , etc.). In all reactions, an excess of energy is transferred not only to kinetic energy of reaction products, but also to excitation of atoms and molecules (e.g., N_2^* , O^* , etc.). In addition, the electronic or vibrational excitation of species can also take place in direct reactions with electrons if they do not possess enough energy for dissociation or ionisation [13]. Reactive species can further undergo mutual post-discharge reactions [14] or react with bulk gas molecules and form more complex long-lived secondary species.

Evaluation of production of gaseous long-lived species by different discharges under various conditions, i.e., the discharge gas-phase chemical activity, have been already studied by many authors experimentally [15, 16] and by numerical modelling [17, 18]. In the air-like mixtures, ozone O_3 and nitrogen oxides NO_x (mainly nitric oxide NO , nitrogen dioxide NO_2 and nitrous oxide N_2O) represent the most frequent long-lived products of atmospheric pressure air discharges [15]. The production of the gaseous species generally depends on discharge parameters (e.g., applied voltage), and working conditions (e.g., composition of a gas mixture) and their formation can be used as a measure of the discharge chemical activity.

In this manuscript, a relatively novel type of discharge, the multi-hollow SDBD (also known as micro-hollow SDBD [19–23]), was investigated. The discharge was generated in a perforated ceramic substrate with the air-exposed electrode. A unique geometry forces the carrier gas to pass through holes (hollows) of the ceramic substrate inside which the discharge is formed. Although the multi-hollow SDBD has been already studied in relevant applications [20, 24–29] and its physical characteristics investigated by several authors [20–22, 30], detailed evaluation of gaseous species produced by the discharge have not been examined yet except for ozone O_3 production [31–33]. Moreover, the NO_x and HNO_3 production promoted by nonthermal plasma have been identified as promising and emerging technology for N_2 fixation under ambient air conditions [34]. In this sense, evaluation of NO_x and HNO_3 produced by the discharge under various working conditions is also important. Therefore, the main objective of this work was to evaluate the gas-phase chemical activity of the multi-hollow SDBD. This research follows our previous work [35] in which the electrical and optical characteristics of the discharge were investigated. Out of the gaseous species produced by the discharge, the production of ozone O_3 , nitrogen oxides NO_x (N_2O , NO , NO_2 , N_2O_5) and nitric acid HNO_3 were evaluated under conditions of various discharge powers (1–5 W), air flow rates (0.25–2.4 L/min) and air relative humidities (0–80%). The effect of air flow rate was examined under dry air conditions, while the effect

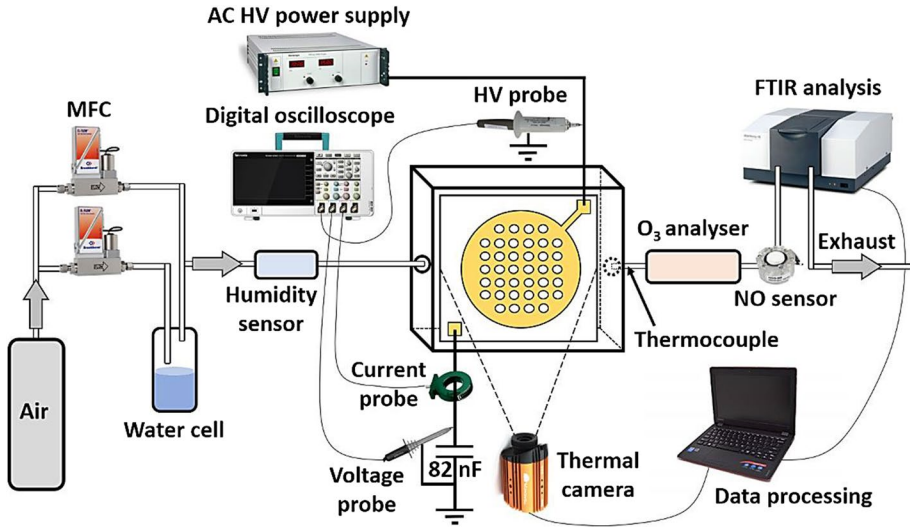


Fig. 1 Experimental setup including discharge reactor and systems for electrical diagnostics and chemical analysis

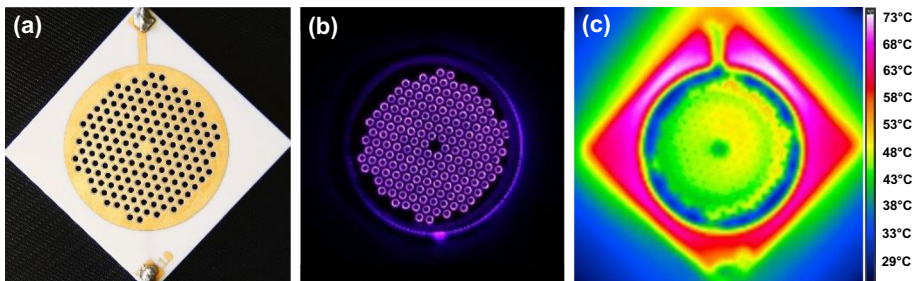


Fig. 2 The photograph of **a** ceramic substrate and **b** multi-hollow SDBD (exposure time 1.6 s, f/5, ISO 800); **c** thermal image of the ceramic substrate during the discharge operation (dry air; discharge power $P = 5$ W; air flow rate $Q = 0.5$ L/min)

of air relative humidity was studied for two air flow rates (0.5 and 1 L/min). In addition, the gas as well as surface temperature of the ceramic substrate were also monitored.

Experimental Setup and Methods

The experimental setup is depicted in Fig. 1. The multi-hollow SDBD was generated in a perforated ceramic square substrate (KD-EB2B10, *Kyocera*) with the dimensions of $50 \times 50 \times 1$ mm (Fig. 2a). It consisted of 170 holes (hollows) with an inner diameter of 1.5 mm and two electrodes—one was embedded inside the ceramic while the other one (made of Ni/Au alloy) was printed on the ceramic surface (air-exposed electrode). More details about the substrate and its parameters can be found in our previous work [35]. The

substrate was powered by AC high voltage (HV) power supply consisting of function generator (*Gwinstek SFG-1013*), signal amplifier (*Omnitronic PAP-350*) and HV transformer. The HV was connected to the air-exposed electrode while the embedded electrode was grounded. Upon application of the AC HV, the discharge was generated at the edge (circumference) of each single hole (Fig. 2b). The waveform of the applied AC HV was measured by HV probe (*Tektronix P6015A*) and the discharge current by a current probe (*Pearson Electronics 2877*) both connected to a digital oscilloscope (*Tektronix TBS2104*). The power consumption of the discharge was evaluated using the Lissajous figure method with an 82 nF capacitor and a voltage probe (*Tektronix P2220*). Synthetic air (purity 5.0) supplied from a pressure tank was used as the carrier gas and its flow rate was controlled by mass flow controllers (MFC) (*Bronkhorst El-Flow Prestige FG-201CV*). The air was alternatively enriched by water vapours by passing it through a water cell. The air relative humidity (RH) was monitored by a capacitive humidity sensor (*Arduino*). Then the air was led into the reactor chamber from the bottom side of ceramic substrate, it passed through the substrate holes, and it exited the substrate by its top side with the air-exposed electrode and left the reactor chamber. At the outlet of the reactor chamber, a thermocouple was placed to measure the gas temperature after passing the discharge zone. Surface temperature of the ceramic substrate was measured by infrared thermal camera (*Workswell WIC2*) (Fig. 2c). Gas-phase chemical activity of the discharge was evaluated by means of FTIR spectroscopy (*Shimadzu IR-Affinity 1S*) with a resolution of 0.5 cm^{-1} inside a gas cell with an optical path length of 10 cm equipped with CaF_2 windows. Main gaseous species (O_3 , N_2O , NO , NO_2 , N_2O_5 , HNO_3) were identified in the FTIR spectra, and their concentrations were evaluated using absorption bands as follows: O_3 at 1055 cm^{-1} ; N_2O at 2236 cm^{-1} ; NO at 1900 cm^{-1} ; NO_2 at 1602 cm^{-1} ; N_2O_5 at 1245 cm^{-1} ; HNO_3 at 1325 cm^{-1} . The absolute concentrations were determined based on calibrations with commercial gas mixtures (NO , NO_2), UV absorption (O_3) or by modelling the spectra (N_2O , N_2O_5 , HNO_3) using a set of absorption lines from HITRAN database (more details can be found in [36]). The approximate detection limits of evaluated species were as follows: 70 ppm for O_3 ; 5 ppm for N_2O ; 70 ppm for NO ; 15 ppm for NO_2 ; 5 ppm for N_2O_5 and 15 ppm for HNO_3 . In addition to FTIR measurements, O_3 concentration was also evaluated by a homemade analyser based on UV absorption at 254 nm using a mercury lamp and the fiber optic emission spectrometer (*Ocean Optics SD2000*) in a 12.5 cm gas cell. The presence of NO was also monitored by an electrochemical sensor (*Membrapor NO/SF-1000*).

In addition to discharge power, the performance of the multi-hollow SDBD was also evaluated with the help of following variables:

- Specific input energy (SIE) (i.e., energy density or discharge energy per gas volume):

$$\text{SIE(J/L)} = \frac{P}{Q}, \quad (1)$$

where P and Q represent discharge power and total air flow rate, respectively.

- Production yield (PY) (i.e., the amount of produced gaseous species per SIE):

$$\text{PY(g/kWh)} = \frac{c}{\text{SIE}} = \frac{Qc}{P}, \quad (2)$$

where c represents the concentration of gaseous species produced by the discharge.

PYs of all evaluated species were calculated for room temperature of $22\text{ }^\circ\text{C}$.

- Production rate (PR) (i.e., the amount of produced gaseous species per unit of time):

$$PR(\text{mg/h}) = Qc. \quad (3)$$

The experiments were performed with applied voltage amplitude in a range of 3.5–6.5 kV at a frequency of 1 kHz resulting in discharge power of 1–5 W. Gas-phase chemical activity of the multi-hollow SDBD was evaluated under conditions of air flow rates in a range of 0.25–2.4 L/min, air RH in a range of 0–80% and the SIE of 25–1200 J/L. Upon application of applied voltage, the temperature of the ceramic substrate gradually increased. Since a production of gaseous species is generally temperature-dependent, their concentrations were measured once the gas temperature and O₃ concentration at the outlet of the reactor chamber were fully stabilised (usually 15–30 min).

Results and Discussion

Figure 3 depicts typical infrared absorption spectra of gaseous species produced by the discharge operated in two distinct modes: “O₃ mode” and “NO_x mode” for the same SIE of 600 J/L (5 W, 0.5 L/min). As we will present in “The Effect of the Air Relative Humidity” section, the presence of humidity in the air can significantly alter the prevailing discharge mode. In the spectra the following absorption bands of the species are denoted: O₃ (1055 and 2125 cm⁻¹), nitrous oxide N₂O (1270 and 2236 cm⁻¹), nitrogen dioxide NO₂ (1627 cm⁻¹), nitric acid HNO₃ (1325 and 1711 cm⁻¹) and dinitrogen pentoxide N₂O₅ (1245 and 1720 cm⁻¹) (Fig. 3).

The Effect of the Air Flow Rate

The gas residence time in the discharge zone can be controlled by varying of gas flow rate. Variation of gas flow rate has a strong impact on gas heating, residual humidity, and gas pre-ionisation and consequently strongly influences the production of gaseous species [20,

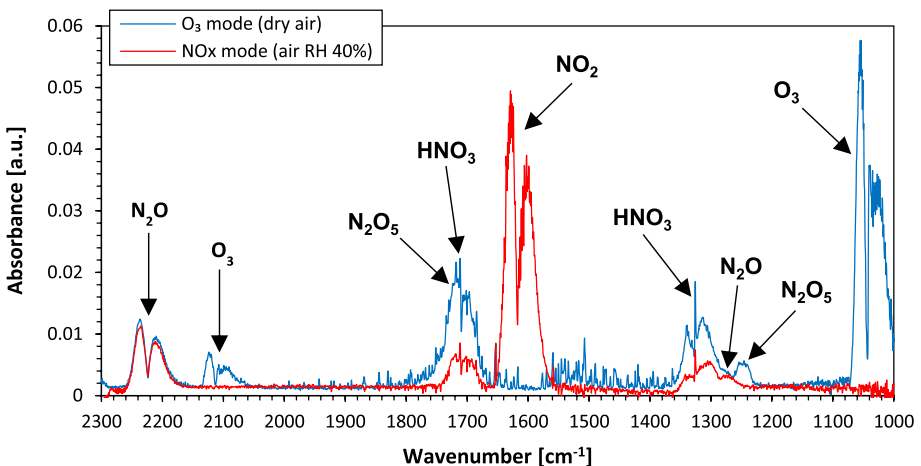
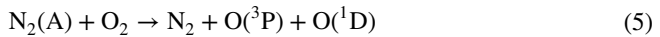
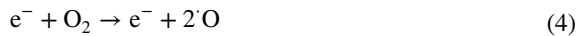


Fig. 3 Infrared absorption spectra of gaseous products of the discharge operated in “O₃ mode” (dry air) and “NO_x mode” (air RH = 40%; SIE = 600 J/L; P = 5 W; Q = 0.5 L/min)

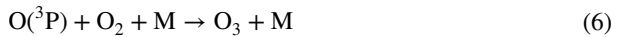
37]. It also affects mixing of produced species and heat exchange in the reaction zone [38]. Therefore, the effect of air flow rate on gas-phase chemical activity of the multi-hollow SDBD was investigated in a range of 0.25–2.4 L/min by using dry air as a carrier gas. The following “Ozone O_3 and Nitrous Oxide N_2O ” section is devoted to the results obtained for O_3 and N_2O . In the “Dinitrogen Pentoxide N_2O_5 and Nitric acid HNO_3 ” section, we present results for N_2O_5 and HNO_3 since they were observed under dry air conditions for all tested air flow rates. Finally, the results for NO and NO_2 can be found in both sections within the discussion on other species, as they were not detected under all conditions tested, but only under the specific ones.

Ozone O_3 and Nitrous Oxide N_2O

Ozone O_3 represents one of the most common gaseous products formed by atmospheric-pressure air DBDs. Production of O_3 is strongly dependent on atomic oxygen species that may be produced by following reactions [18, 39]:



Then, O_3 is produced by a well-known three-body reaction:



where M can be nitrogen N_2 or oxygen O_2 molecule or oxygen atom O [40].

Figure 4a shows the O_3 concentration as a function of discharge power for various dry air flow rates. Since the SIE (energy density) is a very important parameter determining the chemical activity of the discharge and is not constant for a given discharge power and various air flow rates, the concentration of O_3 is also depicted as a function of the SIE (Fig. 4b). The results showed a common feature: an increase of O_3 concentration with a decrease of the air flow rate for a given discharge power (except for air flow rate of 0.25 L/min). The same result for O_3 production by multi-hollow SDBD was also reported by Nayak et al. [32].

Dependence of O_3 concentration on discharge power (or SIE) for a given air flow rate was found nontrivial (Fig. 4). For the air flow rates of 1 and 2.4 L/min the O_3 concentration firstly

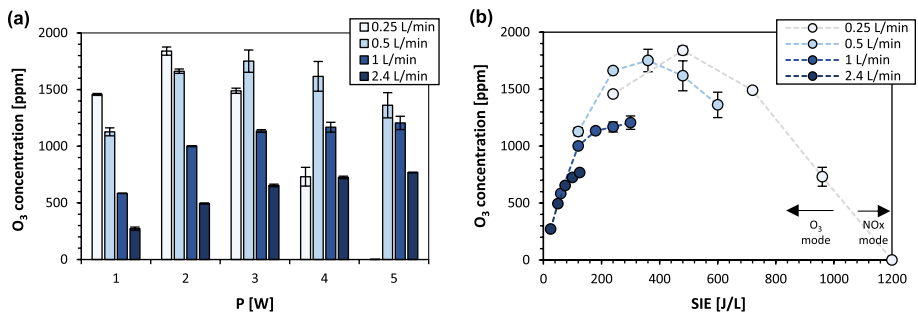


Fig. 4 Concentration of ozone O_3 as a function of **a** discharge power P and **b** specific input energy (SIE) for various air flow rates Q (dry air)

increased and then culminated, whereas for air flow rates of 0.25 and 0.5 L/min, the increase and the culmination were followed by a subsequent decrease of O₃ concentration (Fig. 4). The same trend of O₃ concentration with an increase of DBD power (i.e., the initial increase, culmination, and the following decrease) was also reported by many authors [41–43]. Šimek et al. found a maximum O₃ concentration of 750 ppm for the SIE ~ 110 J/L [43], while we observed the maximum concentration ~ 1840 ppm for much higher SIE of 480 J/L (i.e., 2 W and 0.25 L/min). As is well known, the DBD-based reactors can be operated in two distinct modes. The “O₃ mode” is typical for low SIEs with O₃ dominating among the products. On the other hand, the “NO_x mode” prevails for high SIEs with nitric oxide NO and nitrogen dioxide NO₂ among the products [44, 45].

Production of NO is given by the following set of reactions known as the Zeldovich mechanism [46, 47]:



NO₂ is then formed by subsequent oxidation of NO [48, 49]:



Substantial drop of O₃ concentration to zero for very high SIEs when using dry air flow rate of 0.25 L/min (Fig. 4b) is related to the transition of the discharge from “O₃ mode” to “NO_x mode”. The transition was observed between the SIE of 1000 and 1100 J/L and was characterised by a complete depletion of O₃ associated with an increase of NO and NO₂ [45, 48]. This effect is also known as “discharge poisoning” [50, 51] and will be discussed in detail later.

In addition to O₃, NO and NO₂, nitrous oxide N₂O represents another frequent gaseous product of atmospheric pressure air discharges. Its production and decomposition are predominantly affected by the first excited state of molecular nitrogen N₂(A) via following reactions [52, 53]:



Other reaction pathways leading to N₂O formation are reactions of excited nitrogen atom N(²D) with NO and nitrogen radical ·N with NO₂ [54, 55]:



On the contrary, decomposition of N₂O may happen via reaction with excited oxygen atom O(¹D) [53, 54]:





Unlike O_3 concentration, the N_2O concentration as a function of discharge power (or SIE) and air flow rate was found monotonic when operating the discharge in “ O_3 mode” (i.e., $\text{SIE} < 1000 \text{ J/L}$) (Fig. 5). It increased almost linearly with discharge power and SIE, and significantly decreased with air flow rate. Maximum concentration of 121 ppm was reached for 4 W and 0.25 L/min (i.e., the SIE of 960 J/L). The linear increase of N_2O concentration with the discharge power was also observed in [41, 51] and is probably linked with an increase of the electron energy, what leads to higher production of reactive nitrogen species important for N_2O formation [56]. Tang et al. observed an increase of N_2O concentration with an increase of SIE up to 1500 J/L in a coaxial cylindrical DBD reactor [53]. Above this level a saturated concentration of N_2O was obtained that is related to an equilibrium between the processes of N_2O formation and depletion that are mediated mainly by excited state of molecular nitrogen $\text{N}_2(\text{A})$ (Eqs. 11, 12) and excited oxygen atom $\text{O}(^1\text{D})$ (Eqs. 15, 16). Similar trend in N_2O monotonic increase up to a specific discharge power and following N_2O saturation was also reported in [52]. When using the lowest dry air flow rate (0.25 L/min) and, thus, the highest SIE ($> 1000 \text{ J/L}$), a slight decrease of N_2O concentration was observed (Fig. 5b). This effect may be associated with a transition of the discharge from “ O_3 mode” to “ NO_x mode”. A similar observation was also reported by Kogelschatz and Baessler [51].

Production yields (PYs) of O_3 and N_2O were also calculated (Fig. 6). In contrast to O_3 and N_2O concentrations, they decreased monotonically with the discharge power for all tested air flow rates (except for PY of N_2O for 2.4 L/min that showed a nontrivial trend). The effect of increase of PY of O_3 with an increase of the air flow rate for a given discharge power was also observed by other authors [31, 57]. This may be a result of more efficient cooling of the ceramic substrate. Maximum PYs of O_3 and N_2O were 77.6 and 1.0 g/kWh for the SIE of 25 and 240 J/L, respectively.

To assess “energy effectiveness” of O_3 production by the discharge, the results of our work are compared to those of other authors who used various other types of DBD operated at atmospheric pressure in dry air. Figure 7 presents PY of O_3 as a function of the SIE for all these DBD arrangements. All results presented have the same trend – the PY of O_3 decreases with an increase of SIE. Homola et al. investigated the multi-hollow SDBD with both electrodes embedded inside the ceramic and obtained much higher PY

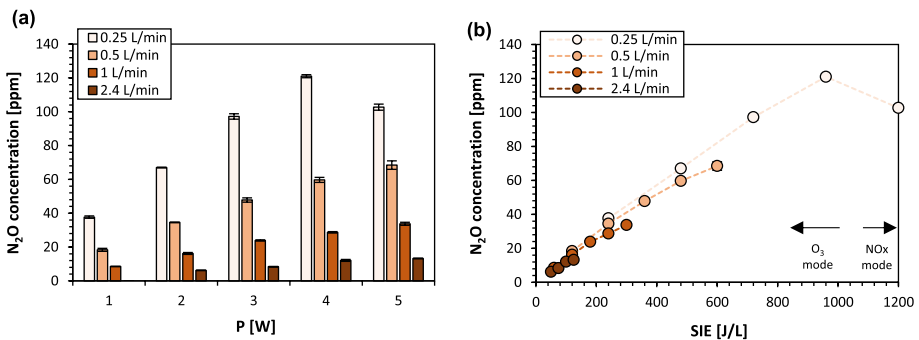


Fig. 5 Concentration of nitrous oxide N_2O as a function of **a** discharge power P and **b** specific input energy (SIE) for various air flow rates Q (dry air)

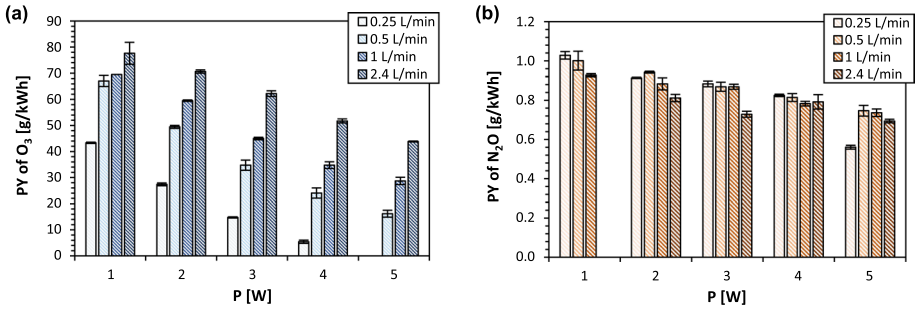
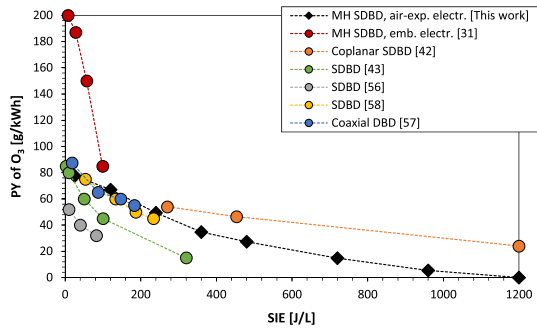


Fig. 6 Production yield (PY) of **a** ozone O_3 and **b** nitrous oxide N_2O as a function of discharge power P for various air flow rates Q (dry air)

Fig. 7 Production yield (PY) of ozone O_3 as a function of specific input energy (SIE). Our results are compared with other DBD arrangements (MH SDBD = multi-hollow surface dielectric barrier discharge; air-exp. electr. = air-exposed electrode; emb. electr. = embedded electrodes)



of O_3 (> 150 g/kWh) than we obtained with the same discharge in configuration with the air-exposed electrode (Fig. 7) [31]. Their PR of O_3 (~ 90 mg/h for PY of 205.5 g/kWh) was comparable with our results (~ 80 mg/h for PY of 77.6 g/kWh). Maximum PR of O_3 we obtained was ~ 220 mg/h for PY of 43.8 g/kWh . The other SDBD reactors are also compared: coplanar SDBD showed higher [42], while the other selected SDBD reactors showed comparable [58] or lower PYs of O_3 [43, 56] than our discharge (Fig. 7). Finally, cylindrical coaxial DBD showed also almost identical results than our discharge [57] (Fig. 7). Lower PY of O_3 obtained with our multi-hollow SDBD compared to its another configuration (embedded electrodes) as well as coplanar SDBD may be related to arrangement of the ceramic substrate itself. The metal electrode exposed to the flowing air could contribute to the catalytic decomposition of O_3 , thereby reducing the PY of O_3 [59]. On the other hand, higher PY of O_3 obtained with our multi-hollow SDBD compared to other SDBD-based reactors could be attributed to the reactor geometry that enables efficient air mixing with generated NTP.

In addition to O_3 , PY of N_2O was also evaluated by Šimek et al. for the SDBD similar to coplanar SDBD and reached ~ 0.8 g/kWh for 250 J/L [43] that can be well compared to our results (~ 1.0 g/kWh for 240 J/L). Besides, maximum PR of N_2O in our experiment reached ~ 3.7 mg/h .

Our results clearly showed that the air flow rate plays an essential role in both O_3 and N_2O production by the discharge. Upon increasing the SIE up to ~ 350 – 500 J/L , O_3 production dominated over O_3 decomposition (Fig. 4b). With further increase of the SIE, the O_3 concentration started to gradually decline implying an increasing influence of O_3

decomposition. Braun et al. proposed that following reactions of O_3 with electrons, O and N species are important for O_3 decomposition under discharge operation [41]:



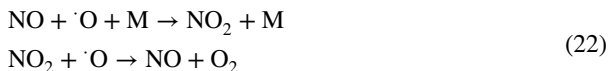
Pekárek and Mikeš [58] and Kim et al. [60] reported the direct electron impact reaction (Eq. 17) as a dominant reaction leading to O_3 decomposition at a gas temperature below 77 °C. Kim et al. [60] further stated that at higher gas temperatures, the recombination of O_3 with O_2 becomes dominant (Eq. 18). Another important O_3 loss reaction especially at higher temperatures is the reaction with excited oxygen atom $O(^1D)$ (Eq. 19) [61]. An increasing effect of both reactions (Eqs. 18, 19) lies in an exponential dependence of their reaction rates on temperature [62, 63]. However, many authors who observed a decrease of O_3 concentration for higher discharge power explained their results referring to the term “ O_3 thermal decomposition” without further explanation. One can also find that reported gas temperature threshold, when O_3 thermal decomposition starts to dominate, varies significantly among the authors. For example, Homola et al. [42] reported a gas temperature of around 80 °C, Osawa and Yoshioka [64] a temperature of 120 °C and Jodzis even temperature above 200 °C. Here, it must be noted that in addition to gas temperature, the temperature in the microdischarge channels should be also considered as it is significantly higher than a gas temperature [61]. In our experiment, we monitored the temperature of both gas and ceramic substrate surface. For the SIE of 600 J/L, the maximum temperatures were almost equal and not too high (~70 °C) [35], so we suppose that temperature is not a dominant factor affecting O_3 decomposition in our case.

Besides the reactions of direct O_3 decomposition presented above, the consumption of $\cdot O$ atoms that are essential for O_3 production must be also taken into account. At higher gas temperatures the $\cdot O$ atoms can be consumed by reactions with N_2 and O_2 molecules (denoted as M):



that may also contribute to the overall decline of O_3 concentration [40, 56]. Based on the discussion above, we suppose that an observed gradual decrease of O_3 concentration from the SIE of 450–500 J/L is given by combination of several factors. Since concentrations of O and N species increase with an increase of the SIE, their reactions with O_3 (Eqs. 19, 20) may play important roles. Other influencing factors are increasing temperature and its effect on reaction rates, as well as increased consumption of $\cdot O$ radicals via reactions with N_2 and O_2 molecules (Eq. 21).

As we have already mentioned, when the SIE exceeded ~1000–1100 J/L, the discharge transition from “ O_3 mode” to “ NO_x mode” was accompanied by a significant change in the composition of produced gaseous species. According to Eliasson and Kogelschatz [48], the transition happens when the NO_x concentration reaches the level at which $\cdot O$ atoms react faster with NO and NO_2 than with O_2 to form O_3 . As a result, an enhanced recombination of $\cdot O$ atoms takes place by the following reaction cycle [50, 51]:



In addition, the previously formed O_3 is effectively consumed by the reaction cycle involving both NO and NO_2 as follows [41, 50]:



As the SIE increases, the vibrationally excited N_2 species start to play a dominant role in formation of NO , which is then a major quencher of O_3 (the first reaction of the cycle Eq. 23) [44, 65]. Since NO and NO_2 concentrations increase with an increase of the SIE and gas temperature [43, 48], the two reaction cycles considerably affect the O_3 concentration especially under conditions of high energy densities ($\text{SIE} > 1000$ J/L). Whereas the first cycle (Eq. 22) contributes to consumption of $\cdot\text{O}$ radicals, the second cycle (Eq. 23) to consumption of O_3 itself. This confirms the role of the reactions Eqs. 19 and 21 in the observed decline of O_3 concentration in dry air under high energy densities (SIE) (Fig. 4b), as the contribution of these reactions is enhanced by a presence of NO and NO_2 .

The maximum concentrations of NO and NO_2 in dry air were 130 and 395 ppm with corresponding PYs of 0.5 and 2.3 g/kWh and PRs of 2.4 and 11 mg/h for 1200 J/L, respectively. It is also important to note that when the discharge was operated in “ O_3 mode” (i.e., $\text{SIE} < 1000$ J/L) regardless of working conditions, NO and NO_2 were not detected in the FTIR spectra.

Dinitrogen Pentoxide N_2O_5 and Nitric Acid HNO_3

Until now, we have discussed the formation of O_3 , N_2O , NO and NO_2 . However, in a strongly oxidising environment, NO_2 can further undergo the oxidation processes promoted by O_3 and $\cdot\text{O}$ as follows [18, 51]:



Consequently, N_2O_5 can be formed via reaction of NO_2 with NO_3 :



Figure 8 show the N_2O_5 concentration as a function of discharge power and SIE for various dry air flow rates. Here it must be noted that N_2O_5 production was not observed for the lowest air flow rate of 0.25 L/min. The maximum concentration of N_2O_5 was 23 ppm (5 W, 1 L/min, 300 J/L). N_2O_5 production was found to increase almost linearly with an increase of discharge power (SIE) (Fig. 8). Unlike the other evaluated compounds in “ O_3 mode” (O_3 , N_2O , HNO_3), a maximum N_2O_5 concentration was observed for a moderate air flow rate of 1 L/min (Fig. 8a). N_2O_5 production by the discharge is generally dependent on several factors including not only discharge power and air flow rate, but also the molar ratio of O_3/NO , geometrical parameters, and temperature of the reactor zone [51, 66]. These factors may explain the observed nontrivial trends of N_2O_5 concentration.

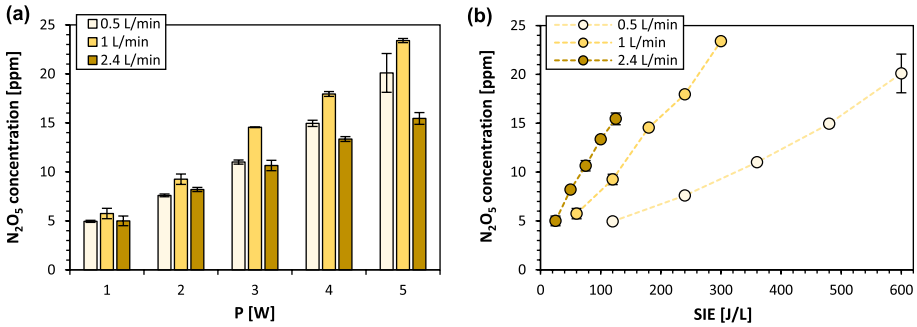
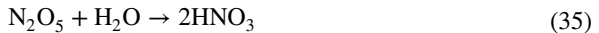
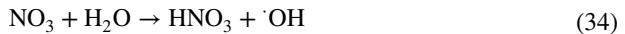
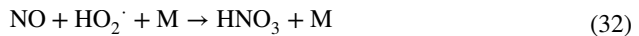
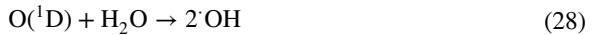


Fig. 8 Concentration of dinitrogen pentoxide N₂O₅ as a function of **a** discharge power P and **b** specific input energy (SIE) for various air flow rates Q (dry air)

In humid air-like mixtures, nitric acid HNO₃ can be also produced by gradual oxidation of NO_x mediated by H, ·OH and HO₂· radicals formed from dissociation of water molecules. The following set of selected reactions can be considered [18, 67]:



Linear trend of HNO₃ production as a function of discharge power and air flow rate (Fig. 9) was similar to that of N₂O production (Fig. 5). In our dry air conditions, only residual (trace) moisture could serve as a source of the radicals (H, ·OH and HO₂·) that mediate HNO₃ production. The same effect of the presence of HNO₃ traces in dry air conditions was also observed by Braun et al. [41]. Upon transition of the discharge from “O₃ mode” to “NO_x mode”, concentration of HNO₃ further slightly increased and reached a maximum of 148 ppm (5 W, 0.25 L/min, 1200 J/L) (Fig. 9a).

PYs of N₂O₅ and HNO₃ are presented in the Fig. 10. Similar to PY of O₃, the PY of N₂O₅ followed the same increasing trend with an increase of air flow rate for a given discharge power (Fig. 10a). A maximum of 3.2 g/kWh was reached for 1 W and 2.4 L/

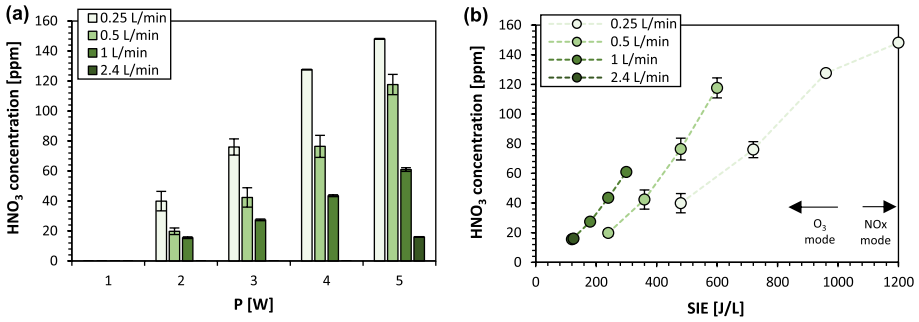


Fig. 9 Concentration of nitric acid HNO₃ as a function of **a** discharge power P and **b** specific input energy (SIE) for various air flow rates Q (dry air)

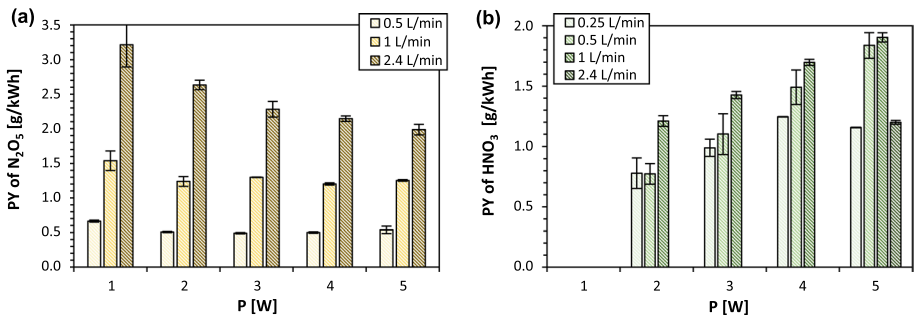


Fig. 10 Production yield (PY) of **a** dinitrogen pentoxide N₂O₅ and **b** nitric acid HNO₃ as a function of discharge power P for various air flow rates Q (dry air)

min (SIE of 25 J/L). It is worth mentioning that for air flow rates of 0.5 and 1 L/min, the PY of N₂O₅ showed almost constant values with an increase of discharge power. Unlike other evaluated compounds, the PY of HNO₃ during discharge operation in “O₃ mode” increased with an increase of discharge power for all tested air flow rates. The maximum of 1.9 g/kWh was found for 5 W and 1 L/min (SIE of 300 J/L) (Fig. 10b). Besides PYs, the PRs of both N₂O₅ and HNO₃ were also evaluated with maxima of ~9.9 and ~9.5 mg/h, respectively.

Here, it must be noted that in order to explain the presence of N₂O₅ and HNO₃ in the FTIR spectra, formation of NO and NO₂ in the “O₃ mode” of the discharge must be considered as they are both precursors for N₂O₅ and HNO₃ formation. As we have already noted, NO and NO₂ were detected only when the discharge was operated in the “NO_x mode”. However, it does not mean they did not form in the “O₃ mode”. We suppose that at least traces of NO and NO₂ were produced in the discharge and their absence in the FTIR spectra indicates either their concentrations below the detection limits or, more probably, their fast consumption by O₃ which is a dominant product of the discharge in the “O₃ mode” (Eqs. 10, 24) [43, 56]. The second effect could be even more pronounced as the FTIR spectrometer was placed in some distance from the reactor chamber. Once the air came to the gas cell, NO and NO₂ were already consumed very probably by O₃. Additionally, to monitor NO the electrochemical sensor was placed just behind the reactor chamber. However, even the sensor did not detect any NO, thus confirming its fast consumption in

the discharge in the “O₃ mode”. Consequently, NO₂ and NO₃ may further react and form N₂O₅ (Eq. 26) or even HNO₃ (Eq. 35) if at least a trace humidity is present. Braun et al. reported that when a large surplus of O₃ is present especially at low gas temperatures, the equilibrium of Eq. 26 is shifted almost completely towards N₂O₅ without detection of NO₂ and NO₃ what corresponds with our results [41]. The same absence of NO and NO₂ was also observed by Abdelaziz et al. when using SDBD-based reactor [56]. Hence, we can conclude that the gaseous species produced by the multi-hollow SDBD operated in the “O₃ mode” include O₃, N₂O, N₂O₅ and HNO₃. When the discharge is transitioned to the “NO_x mode”, in addition to N₂O and HNO₃, NO and NO₂ are also present. The observed concentrations of O₃, N₂O and N₂O₅ in the “O₃ mode” agree with the typical feature of this mode reported by Eliasson and Kogelschatz [48]: the O₃ concentration was roughly two orders of magnitude higher than the concentrations of N₂O and N₂O₅.

The Effect of the Air Relative Humidity

Humidity of a gas mixture affects the discharge from many aspects. It influences not only the physical processes of discharge formation, propagation, and its characteristics [68, 69], but also it substantially affects and alters the plasma chemistry [67, 70]. To evaluate the effect of air humidity on gas-phase chemical activity of the multi-hollow SDBD, experiments were performed for various air relative humidity (RH) levels of 20, 40, 60 and 80% at atmospheric pressure with a constant room temperature of ~22°C, so the absolute humidity of the air (water content) was 3.9, 7.8, 11.7, 15.6 g/m³, respectively. The effect of humidity was studied for a fixed air flow rate of 1 L/min and discharge powers of 1–5 W, so the maximum SIE was 300 J/L. Under these conditions, the discharge was operated only in the “O₃ mode”. Decreasing the air flow rate to 0.5 L/min allowed the transition of the discharge to “NO_x mode” with the maximum SIE of 600 J/L.

Ozone O₃ and Nitrous Oxide N₂O

Figure 11a shows the O₃ concentration as a function of discharge power for various air RHs. Our results confirmed a well-known fact that production of O₃ by the discharges significantly decreases with any impurity in the gas mixture including water H₂O, hydrocarbons, etc. [57, 71]. A decrease of O₃ concentration was found non-linear. It means that the rate of O₃ concentration decrease is greater for low than for high levels of air RH (Fig. 11a).

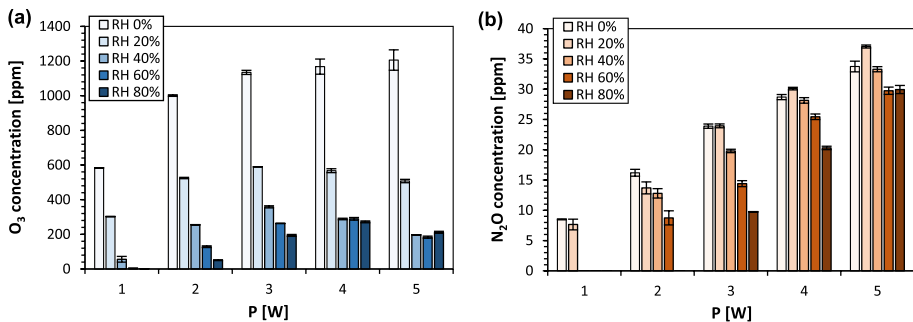


Fig. 11 Concentration of **a** ozone O₃ and **b** nitrous oxide N₂O as a function of discharge power *P* for various air relative humidities (RH) (*Q* = 1 L/min)

A non-linear decrease of O_3 production was also reported by Chen and Wang when investigating DC corona discharge in humid air [70]. The significant decrease of O_3 concentration when water vapour is present can be explained by the consumption of $\cdot O$ radicals triggered by $HO_2\cdot$ and $\cdot OH$ radicals formed from dissociation of H_2O and O_2 molecules:



or by reaction with water (Eq. 28) [57, 70]. Thus, consumption of $\cdot O$ radicals accelerates with an increase of air humidity leading to lower O_3 production. Decline in formation of $\cdot O$ radicals can also be caused by a reduction in electron density due to an electronegativity of water molecules [67]. In addition, humidity also accelerates the relaxation rate of the vibration-to-translation of N_2 and O_2 molecules leading to the decline of O as well as N excited species [67]. Another possible pathway for O_3 consumption may be by direct reactions of O_3 with $\cdot OH$ and $\cdot H$ radicals [70, 72]:



When the reaction of $\cdot H$ with O_3 (Eq. 39) is followed by the reaction of $\cdot OH$ with $\cdot O$ (Eq. 37), giving the net reaction of $\cdot O$ with O_3 (Eq. 19), the $\cdot H$ and $\cdot OH$ radicals can act as a “catalyst” to reduce O_3 concentration (similar to NO_x in the reaction cycle Eq. 23) [72].

Figure 11b shows N_2O concentration as a function of discharge power for various air RHs. For low discharge powers (<2 W), the maximum concentration of N_2O was obtained in dry air, while for higher discharge powers (>4 W), it was reached in air with RH of 20% (Fig. 11b). In general, production of nitrogen excited species $N_2(A)$ important for N_2O production decreases with an increase of air humidity. This is due to very efficient quenching of $N_2(A)$ species by water molecules [49]. This explains a decrease of N_2O concentration when increasing the air RH from 20 to 80%. However, an increase of N_2O concentration with air RH from 0 to 20% for 4 and 5 W may indicate that other reactions leading to N_2O formation may also play important roles under these specific conditions. Abdelaziz et al. [67] and Matsui et al. [73] observed an increase of NO and NO_2 concentrations upon increasing the air humidity, so the reactions of N_2O formation moderated by NO and NO_2 (Eqs. 13, 14) may dominate.

In addition to O_3 and N_2O concentrations, their corresponding PYs were also evaluated (Fig. 12). Similar to O_3 concentration, the PY of O_3 followed the same trend with an increase of air RH: it significantly decreased for a given discharge power (Fig. 12a). Moreover, in air with RH higher than 40%, the increasing humidity had no effect on PY of O_3 for the highest tested discharge powers (4 and 5 W). In addition, the PY of N_2O followed a trend similar to the concentration reaching maximum values in dry air (for 1 and 2 W) or in air with RH of 20% (for 4 and 5 W) (Fig. 12b).

Dinitrogen Pentoxide N_2O_5 and Nitric Acid HNO_3

In humid air, N_2O_5 was not detected in the FTIR spectra regardless of discharge power and air flow rate. Similar observations were also reported by other authors [41, 51]. This

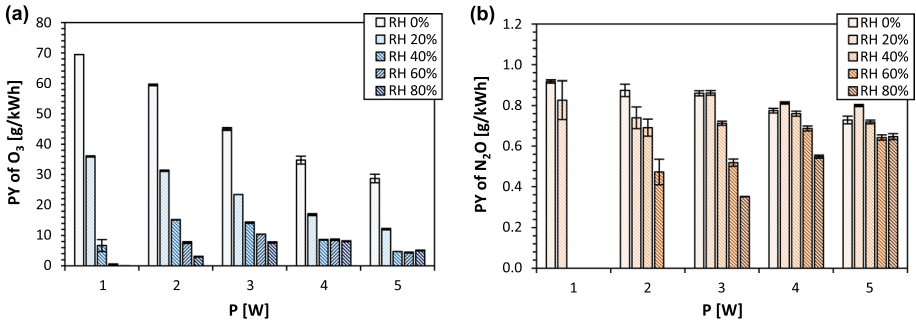


Fig. 12 Production yield (PY) of **a** ozone O₃ and **b** nitrous oxide N₂O as a function of discharge power P for various air relative humidities (RH) ($Q = 1$ L/min)

can be explained by the complete consumption of N₂O₅ by reaction with H₂O leading to the formation of HNO₃ (Eq. 35).

Figure 13a shows the HNO₃ concentration as a function of discharge power for various air RHs. It initially increased with an increase of air RH from 0 to 40%, but with its further increase, the concentration of HNO₃ declined. The initial increase of HNO₃ concentration can be easily explained, as precursors to its production (radicals $\cdot\text{H}$, $\cdot\text{OH}$, HO₂) are expected to rise with an increase of humidity [49]. In this sense, the decline of HNO₃ concentration at air RH > 40% seems counterintuitive. Similar trend of HNO₃ concentration increase followed by a decline was also observed by Matsui et al. [73] with a maximum concentration at air RH of 30%. They suggested that at higher air RH, HNO₃ produced by the discharge can be easily absorbed by the water which is previously adsorbed on the inner surface of the connecting tubes due to its high miscibility. If HNO₃ is absorbed by the water inside the experimental system before it enters the gas cell, it may cause a decline of HNO₃ in the measured spectra [67]. In addition to concentration, the PY of HNO₃ followed a similar trend (Fig. 13b). The highest concentration of HNO₃ was 142 ppm corresponding to PY of 4.4 g/kWh (air RH 40%, 300 J/L).

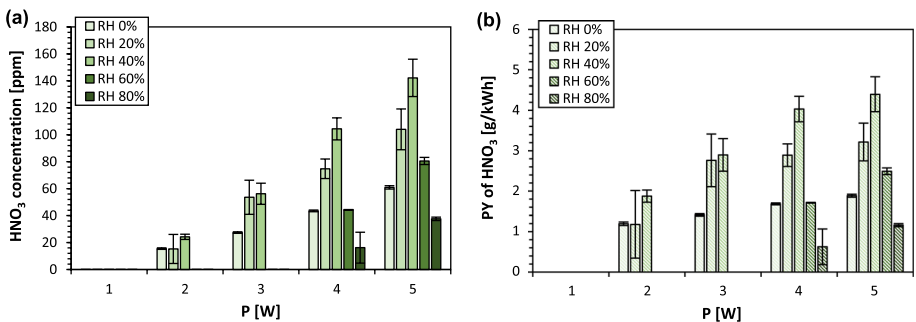


Fig. 13 **a** Concentration and **b** production yield (PY) of nitric acid HNO₃ as a function of discharge power P for various air relative humidities (RH) ($Q = 1$ L/min)

Transition of the Discharge from “O₃ Mode” to “NO_x Mode” at Higher Humidities

In a previous section, the effect of air RH on production of gaseous species by the discharge was evaluated for air flow rate of 1 L/min and maximum SIE of 300 J/L, i.e., under “O₃ mode” conditions. To investigate the effect of air RH on transition of the discharge from “O₃ mode” to “NO_x mode”, the SIE must be further increased. Therefore, the air flow rate was decreased to 0.5 L/min obtaining the SIE up to 600 J/L.

The results showed that the air RH has a significant impact on the SIE value for the transition between the two discharge modes. Figure 14 show concentrations of O₃, N₂O, HNO₃ and NO₂ as a function of discharge power (or SIE) in air with various relative humidities (20–80%). According to these results it can be concluded that a presence of humidity substantially decreases the SIE value for transition between the two discharge modes. In dry air, the transition from “O₃ mode” to “NO_x mode” was found between 1000 and 1100 J/L. In air with RH of 20 and 40%, the transition was observed between 500 and 600 J/L (Fig. 14a, b), while in air with RH of 60 and 80%, it was found around 450 J/L (Fig. 14c, d). In humid air under “NO_x mode” conditions, NO was not found in the FTIR spectra. Although we did not observe it, it does not mean that it was not produced. In humid air, the radicals formed by water dissociation (·OH, HO₂·) can mediate formation of NO through the following reactions [67]:

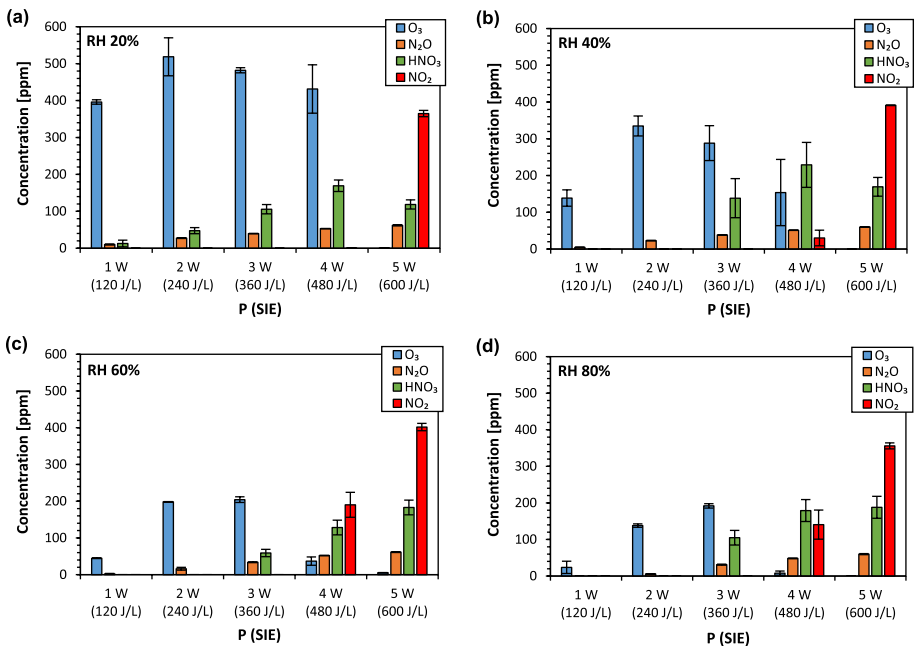


Fig. 14 Concentrations of O₃, N₂O, HNO₃ and NO₂ as a function of discharge power *P* or specific input energy (SIE) for various air relative humidities (RH): **a** 20%; **b** 40%; **c** 60%; and **d** 80% (*Q* = 0.5 L/min)

These reactions can compensate for decreasing production of NO through reactions where $\cdot\text{N}$, $\cdot\text{O}$ and $\text{N}_2(\text{A})$ are involved [49]. Moreover, NO can further undergo an oxidation to NO_2 or HNO_3 promoted by $\cdot\text{O}$, O_3 and $\text{HO}_2\cdot$ (Eqs. 9, 10, 31, 32). Therefore, we suppose that absence of NO and presence of NO_2 and HNO_3 in the FTIR spectra in humid air under “ NO_x mode” conditions may indicate fast consumption of NO to higher oxidation products NO_2 and HNO_3 probably mediated by $\cdot\text{OH}$ and $\text{HO}_2\cdot$ radicals. The maximum NO_2 concentrations were found in a range of 350–402 ppm for the SIE of 600 J/L (Fig. 14) with corresponding PYs of 4–4.6 g/kWh and PRs of 20–23 mg/h, respectively. Concentration of HNO_3 reached maximum of 229 ppm at air RH of 40% for 480 J/L (Fig. 14b) with PY of 4.5 g/kWh and PR of 17.9 mg/h. These results indicate that humid air promoted a production of NO_2 and HNO_3 compared to their production in dry air for the same air flow rate (0.5 L/min). A similar effect was also observed by Baerdemaeker et al. [74] using multi-hollow SDBD with both electrodes embedded inside the ceramic.

To explain decreasing SIE value for transition between the two discharge modes with an increase of air RH, one must consider the O_3/NO_x ratio. In the “ O_3 mode”, the O_3/NO_x ratio is typically very high ($\gg 1$) as O_3 dominates the products. On the other hand, in the “ NO_x mode” the ratio is typically low (< 1) due to very low O_3 concentration. Our results showed that the O_3 concentration substantially decreased upon increasing the air RH. Therefore, the increase of humidity can significantly decrease the O_3/NO_x ratio and, thus, may promote the transition between the discharge modes for lower SIE in contrast to dry air.

Conclusions

Evaluation of the gaseous species production by the discharge, i.e., the discharge chemical activity, is one of the key factors for its effective employment for practical applications. In this manuscript, the gas-phase chemical activity of the multi-hollow surface dielectric barrier discharge generated in a perforated ceramic substrate with an air-exposed electrode was presented. The unique discharge geometry allowed the carrier gas to pass through holes (hollows) of the substrate and, thus, enabled efficient production of gaseous species. The production of ozone O_3 , nitrous oxide N_2O , nitric oxide NO, nitrogen dioxide NO_2 , dinitrogen pentoxide N_2O_5 and nitric acid HNO_3 was evaluated in terms of concentration (ppm), production yield (PY in g/kWh) and production rate (PR in mg/h) under conditions of various discharge powers (1–5 W), air flow rates (0.25–2.4 L/min) and air relative humidities (RH; 0–80%). The effect of air flow rate was examined under dry air conditions, while the effect of air RH was studied for two air flow rates (0.5 and 1 L/min).

The work demonstrated a critical impact of both the air flow rate and the relative humidity on the prevailing discharge mode (“ O_3 mode” vs. “ NO_x mode”) and, thus, on production and composition of the gaseous species. Whereas the air flow rate determines the gas residence time in a discharge zone and gas heating, the air relative humidity influences the discharge from physical (processes of discharge formation, propagation, and its characteristics) as well as chemical (production of $\cdot\text{H}$, $\cdot\text{OH}$, $\text{HO}_2\cdot$ radicals) aspects. When the discharge was operated in the “ O_3 mode”, O_3 , N_2O , N_2O_5 and HNO_3 were observed among the gaseous products, while in the “ NO_x mode”, N_2O , HNO_3 , NO and NO_2 were present.

In dry air, the results showed that the concentrations of O_3 , N_2O and HNO_3 increase with a decrease of the air flow rate for a given discharge power, except for the lowest tested air flow rate (0.25 L/min) due to the discharge mode transition. On the contrary,

the concentration of N_2O_5 was found the highest for the moderate air flow rate of 1 L/min (23 ppm with corresponding PY of 1.2 g/kWh for 300 J/L). Moreover, concentrations of N_2O , HNO_3 and N_2O_5 monotonously increased with an increase of discharge power in “ O_3 mode”, while concentration of O_3 showed a nontrivial trend for 0.25 and 0.5 L/min. Upon increasing the discharge power or specific input energy (SIE), the O_3 concentration firstly increased, culminated, and then gradually declined, or eventually dropped down to zero (for 0.25 L/min). A complete depletion of O_3 was related to the discharge transition from “ O_3 mode” to “ NO_x mode” associated with an increase of NO and NO_2 with maximum concentrations of 130 and 395 ppm with corresponding PYs of 0.5 and 2.3 g/kWh for 1200 J/L, respectively. The maximum O_3 concentration was 1840 ppm with corresponding PY of 27 g/kWh for 480 J/L, whereas the maximum PY of O_3 (78 g/kWh) was reached at concentration of 272 ppm for 25 J/L. For a comparison, the maximum N_2O concentration was 121 ppm with corresponding PY of 0.8 g/kWh for 960 J/L.

In humid air, the O_3 concentration substantially decreased with an increase of air RH for a given discharge power and a rate of reduction was larger for low than for high levels of air RH. The N_2O concentration showed more complicated trend: for low discharge powers (< 2 W), the maximum concentration was obtained in dry air, while for higher discharge powers (> 4 W), it was reached in air with RH of 20%. Further, the maximum HNO_3 concentration (142 ppm) was observed at air RH of 40% with corresponding PY of 4.4 g/kWh for 300 J/L. On the other hand, N_2O_5 was not detected at all under humid air conditions.

Overall, the results showed that a presence of air humidity substantially decreases the SIE (energy density) value for discharge transition from “ O_3 mode” to “ NO_x mode”. In dry air, a transition was found between 1000 and 1100 J/L, while with an increase of air RH from 20 to 80%, it gradually decreased from approximately 600 to 450 J/L, respectively. We suppose that upon increasing the humidity a decrease of O_3/NO_x ratio may be responsible for the observed effect.

The work demonstrated that the multi-hollow surface dielectric barrier discharge is capable of production of various gaseous species in a wide range of concentrations that can be controlled by proper discharge operating conditions. Therefore, we suppose the discharge may eventually find many possible applications, particularly in plasma pollution control and biomedicine.

Acknowledgements This work was supported by Slovak Research and Development Agency Grants APVV-20-0566 and APVV-17-0382, and Slovak Grant Agency VEGA 1/0822/21.

Authors' Contributions Both authors contributed to the study conception and design. Experiments, analyses, data collection and processing were performed by R.C. The first draft of the manuscript was written by R.C. Revision of the draft of the manuscript was performed by K.H. Both authors read and approved the final manuscript.

Funding Open access funding provided by The Ministry of Education, Science, Research and Sport of the Slovak Republic in cooperation with Centre for Scientific and Technical Information of the Slovak Republic. As stated in the Acknowledgement, this work was supported by Slovak Research and Development Agency grants APVV-20-0566 and APVV-17-0382, and Slovak Grant Agency VEGA 1/0822/21.

Availability of Data and Materials The data that support the findings of this study are available from the corresponding author upon reasonable request.

Declarations

Conflict of interests The authors have no competing interests to declare that are relevant to the content of this article.

Ethical Approval This declaration is “not applicable”.

Open Access This article is licensed under a Creative Commons Attribution 4.0 International License, which permits use, sharing, adaptation, distribution and reproduction in any medium or format, as long as you give appropriate credit to the original author(s) and the source, provide a link to the Creative Commons licence, and indicate if changes were made. The images or other third party material in this article are included in the article's Creative Commons licence, unless indicated otherwise in a credit line to the material. If material is not included in the article's Creative Commons licence and your intended use is not permitted by statutory regulation or exceeds the permitted use, you will need to obtain permission directly from the copyright holder. To view a copy of this licence, visit <http://creativecommons.org/licenses/by/4.0/>.

References

1. Cvelbar U, Walsh JL, Černák M et al (2019) White paper on the future of plasma science and technology in plastics and textiles. *Plasma Process Polym* 16:1–37. <https://doi.org/10.1002/ppap.201700228>
2. Šimek M, Černák M, Kylián O et al (2019) White paper on the future of plasma science for optics and glass. *Plasma Process Polym* 16:1–23. <https://doi.org/10.1002/ppap.201700250>
3. Corke TC, Enloe CL, Wilkinson SP (2010) Dielectric barrier discharge plasma actuators for flow control. *Annu Rev Fluid Mech* 42:505–529. <https://doi.org/10.1146/annurev-fluid-121108-145550>
4. Boeuf JP, Pitchford LC (2005) Electrohydrodynamic force and aerodynamic flow acceleration in surface dielectric barrier discharge. *J Appl Phys* 97:103307. <https://doi.org/10.1063/1.1901841>
5. Hackam R, Akiyama H (2000) Air pollution control by electrical discharges. *IEEE Trans Dielectr Electr Insul* 7:654–683. <https://doi.org/10.1109/94.879361>
6. Magureanu M, Bradu C, Parvulescu VI (2018) Plasma processes for the treatment of water contaminated with harmful organic compounds. *J Phys D Appl Phys* 51:313002. <https://doi.org/10.1088/1361-6463/aacd9c>
7. Machala Z, Hensel K, Akishev Y (2012) *Plasma for bio-decontamination, medicine and food security*. NATO Science for Peace and Security Series A—Chemistry and Biology, Springer, Dordrecht
8. Moreau M, Orange N, Feuilloley MJG (2008) Non-thermal plasma technologies: new tools for bio-decontamination. *Biotechnol Adv* 26:610–617. <https://doi.org/10.1016/j.biotechadv.2008.08.001>
9. Weltmann KD, Von Woedtke T (2017) Plasma medicine—current state of research and medical application. *Plasma Phys Control Fusion* 59:14031. <https://doi.org/10.1088/0741-3335/59/1/014031>
10. Fridman G, Friedman G, Gutsol A et al (2008) Applied plasma medicine. *Plasma Process Polym* 5:503–533. <https://doi.org/10.1002/ppap.200700154>
11. Puač N, Gherardi M, Shiratani M (2018) Plasma agriculture: a rapidly emerging field. *Plasma Process Polym* 15:1–5. <https://doi.org/10.1002/ppap.201700174>
12. Kogelschatz U (2003) Dielectric-barrier discharges: their history, discharge physics, and industrial applications. *Plasma Chem Plasma Process* 23:1–46. <https://doi.org/10.1023/A:1022470901385>
13. Fridman A (2008) *Plasma Chemistry*. Cambridge University Press
14. Ono R (2016) Optical diagnostics of reactive species in atmospheric-pressure nonthermal plasma. *J Phys D Appl Phys* 49:83001. <https://doi.org/10.1088/0022-3727/49/8/083001>
15. Liu K, Zheng Z, Liu S, Hu Y (2019) Study on the physical and chemical characteristics of DBD: the effect of N₂/O₂ mixture ratio on the product regulation. *Plasma Chem Plasma Process* 39:1255–1274. <https://doi.org/10.1007/s11090-019-09998-1>
16. Pavlovich MJ, Clark DS, Graves DB (2014) Quantification of air plasma chemistry for surface disinfection. *Plasma Sources Sci Technol* 23:065036. <https://doi.org/10.1088/0963-0252/23/6/065036>
17. Eliasson B, Egli W, Kogelschatz U (1994) Modelling of dielectric barrier discharge chemistry. *Pure Appl Chem* 66:1275–1286. <https://doi.org/10.1351/pac199466061275>
18. Peyrou R (1990) The effect of relative humidity on ozone production by corona discharge in oxygen or air—a numerical simulation—Part II: Air. *Ozone Sci Eng* 12:41–64. <https://doi.org/10.1080/01919519008552454>
19. Homola T, Krumpolec R, Zemánek M et al (2017) An array of micro-hollow surface dielectric barrier discharges for large-area atmospheric-pressure surface treatments. *Plasma Chem Plasma Process* 37:1149–1163. <https://doi.org/10.1007/s11090-017-9792-z>
20. Nayak G, Du Y, Brandenburg R, Bruggeman PJ (2017) Effect of air flow on the micro-discharge dynamics in an array of integrated coaxial microhollow dielectric barrier discharges. *Plasma Sources Sci Technol* 26:035001. <https://doi.org/10.1371/journal.pone.0080705>

21. Sakai O, Kishimoto Y, Tachibana K (2005) Integrated coaxial-hollow micro dielectric-barrier-discharges for a large-area plasma source operating at around atmospheric pressure. *J Phys D Appl Phys* 38:431–441. <https://doi.org/10.1088/0022-3727/38/3/012>
22. Tachibana K, Nakamura T, Motomura H (2016) Monolithic structure of integrated coaxial micro-hollow dielectric barrier discharges: Characterization for environmental and biomedical applications. *Jpn J Appl Phys* 55:07LB01. <https://doi.org/10.7567/JJAP.55.07LB01>
23. Čimerman R, Hensel K (2021) Generation of honeycomb discharge assisted by micro-hollow surface dielectric barrier discharge. *Int J Plasma Environ Sci Technol* 15:e01003. <https://doi.org/10.34343/ijpest.2021.15.e01003>
24. Krumpolec R, Richter V, Zemánek M, Homola T (2019) Multi-hollow surface dielectric barrier discharge for plasma treatment of patterned silicon surfaces. *Surf Interfaces* 16:181–187. <https://doi.org/10.1016/j.surf.2019.01.014>
25. Nayak G, Aboubakr HA, Goyal SM, Bruggeman PJ (2017) Reactive species responsible for the inactivation of feline calicivirus by a two-dimensional array of integrated coaxial microhollow dielectric barrier discharges in air. *Plasma Process Polym* 15:1–12. <https://doi.org/10.1002/ppap.201700119>
26. Aboubakr HA, Nisar M, Nayak G et al (2020) Bactericidal efficacy of a two-dimensional array of integrated, coaxial, microhollow, dielectric barrier discharge plasma against *Salmonella enterica* Serovar Heidelberg. *Foodborne Pathog Dis* 17:157–165. <https://doi.org/10.1089/fpd.2019.2698>
27. Kelar Tučeková Z, Vacek L, Krumpolec R et al (2021) Multi-hollow surface dielectric barrier discharge for bacterial biofilm decontamination. *Molecules* 26:910. <https://doi.org/10.3390/molecules26040910>
28. Gebremical GG, Admassu S, Berhanu T et al (2019) Optimization and influence of multi-hollow surface dielectric barrier discharge plasma operating conditions on the physical quality of peanut. *Eur Phys J D* 73:1–16. <https://doi.org/10.1140/epjd/e2019-90616-0>
29. Gebremical GG, Emire SA, Berhanu T (2019) Effects of multihollow surface dielectric barrier discharge plasma on chemical and antioxidant properties of peanut. *J Food Qual* 2019:3702649. <https://doi.org/10.1155/2019/3702649>
30. Shimizu K, Ishii T, Blajan M (2010) Emission spectroscopy of pulsed power microplasma for atmospheric pollution control. *IEEE Trans Ind Appl* 46:1125–1131. <https://doi.org/10.1109/TIA.2010.2044968>
31. Homola T, Prukner V, Hoffer P, Šimek M (2020) Multi-hollow surface dielectric barrier discharge: an ozone generator with flexible performance and supreme efficiency. *Plasma Sources Sci Technol* 29:095014. <https://doi.org/10.1088/1361-6595/aba987>
32. Nayak G, Sousa JS, Bruggeman PJ (2017) Singlet delta oxygen production in a 2D micro-discharge array in air: effect of gas residence time and discharge power. *J Phys D Appl Phys* 50:105205. <https://doi.org/10.1088/1361-6463/aa5764>
33. Voráč J, Britun N, Nikiforov A et al (2019) Photofragmentation laser-induced fluorescence of ozone: an in situ tool for precise mapping of ozone concentration in non-thermal plasmas. *Appl Phys Express* 12:106001. <https://doi.org/10.7567/1882-0786/ab3d15>
34. Cherkasov N, Ibadon AO, Fitzpatrick P (2015) A review of the existing and alternative methods for greener nitrogen fixation. *Chem Eng Process* 90:24–33. <https://doi.org/10.1016/j.ccep.2015.02.004>
35. Čimerman R, Maťaš E, Sárený M, Hensel K (2022) Electrical and optical characterization of multi-hollow surface dielectric barrier discharge in configuration with the air-exposed electrode. *Phys Plasmas* 29:113510. <https://doi.org/10.1063/5.0101496>
36. Janda M, Hensel K, Tóth P et al (2021) The role of HNO₂ in the generation of plasma-activated water by air transient spark discharge. *Appl Sci* 11:7053. <https://doi.org/10.3390/app11157053>
37. Höft H, Becker MM, Kettlitz M (2016) Impact of gas flow rate on breakdown of filamentary dielectric barrier discharges. *Phys Plasmas* 23:033504. <https://doi.org/10.1063/1.4943278>
38. Jodzis S, Smoliński T, Sówka P (2011) Application of a concentric actuator for ozone synthesis under surface discharge conditions. *IEEE Trans Plasma Sci* 39:1055–1060. <https://doi.org/10.1109/TPS.2011.2105285>
39. Chen J, Davidson JH (2002) Ozone production in the positive DC corona discharge: model and comparison to experiments. *Plasma Chem Plasma Process* 22:495–522. <https://doi.org/10.1023/A:1021315412208>
40. Zhang Y, Liang X, Xu M, Wei L (2018) Energy conversion and temperature dependence in ozone generator fed by synthetic air. *Ozone Sci Eng* 40:361–371. <https://doi.org/10.1080/01919512.2018.1431520>
41. Braun D, Kuchler U, Pietsch G (1988) Behaviour of NO_x in air-fed ozonizers. *Pure Appl Chem* 60:741–746. <https://doi.org/10.1351/pac198860050741>

42. Homola T, Pongráč B, Zemánek M, Šimek M (2019) Efficiency of ozone production in coplanar dielectric barrier discharge. *Plasma Chem Plasma Process* 39:1227–1242. <https://doi.org/10.1007/s11090-019-09993-6>
43. Šimek M, Pekárek S, Prukner V (2012) Ozone production using a power modulated surface dielectric barrier discharge in dry synthetic air. *Plasma Chem Plasma Process* 32:743–754. <https://doi.org/10.1007/s11090-012-9382-z>
44. Shimizu T, Sakiyama Y, Graves DB et al (2012) The dynamics of ozone generation and mode transition in air surface micro-discharge plasma at atmospheric pressure. *New J Phys* 14:103028. <https://doi.org/10.1088/1367-2630/14/10/103028>
45. Kogelschatz U, Eliasson B, Hirth M (1988) Ozone generation from oxygen and air: discharge physics and reaction mechanisms. *Ozone Sci Eng* 10:367–377. <https://doi.org/10.1080/01919518808552391>
46. Machala Z, Tarabová B, Sersenová D et al (2019) Chemical and antibacterial effects of plasma activated water: correlation with gaseous and aqueous reactive oxygen and nitrogen species, plasma sources and air flow conditions. *J Phys D Appl Phys* 52:034002. <https://doi.org/10.1088/1361-6463/aae807>
47. Pawlat J, Terebun P, Kwiatkowski M et al (2019) Evaluation of oxidative species in gaseous and liquid phase generated by mini-gliding Arc discharge. *Plasma Chem Plasma Process* 39:627–642. <https://doi.org/10.1007/s11090-019-09974-9>
48. Eliasson B, Kogelschatz U (1991) Modeling and applications of silent discharge plasmas. *IEEE Trans Plasma Sci* 19:309–323. <https://doi.org/10.1109/27.106829>
49. van Gaens W, Bogaerts A (2014) Reaction pathways of biomedically active species in an Ar plasma jet. *Plasma Sources Sci Technol* 23:035015. <https://doi.org/10.1088/0963-0252/23/3/035015>
50. Pekárek S (2011) Effect of catalysts on dc corona discharge poisoning. *Eur Phys J D* 61:657–662. <https://doi.org/10.1140/epjd/e2010-10246-4>
51. Kogelschatz U, Baessler P (1987) Determination of nitrous oxide and dinitrogen pentoxide concentrations in the output of air-fed ozone generators of high power density. *Ozone Sci Eng* 9:195–206. <https://doi.org/10.1080/01919518708552335>
52. Fan X, Kang S, Li J, Zhu T (2018) Formation of nitrogen oxides (N₂O, NO, and NO₂) in typical plasma and plasma-catalytic processes for air pollution control. *Water Air Soil Pollut* 229:351. <https://doi.org/10.1007/s11270-018-4011-y>
53. Tang X, Wang J, Yi H et al (2017) N₂O formation characteristics in dielectric barrier discharge reactor for environmental application: effect of operating parameters. *Energy Fuels* 31:13901–13908. <https://doi.org/10.1021/acs.energyfuels.7b02428>
54. Kučerová K, Machala Z, Hensel K (2020) Transient spark discharge generated in various N₂/O₂ gas mixtures: reactive species in the gas and water and their antibacterial effects. *Plasma Chem Plasma Process* 40:749–773. <https://doi.org/10.1007/s11090-020-10082-2>
55. Teodoru S, Kusano Y, Bogaerts A (2012) The effect of O₂ in a humid O₂/N₂/NO_x gas mixture on NO_x and N₂O remediation by an atmospheric pressure dielectric barrier discharge. *Plasma Processes Polym* 9:652–689. <https://doi.org/10.1002/ppap.201100187>
56. Abdelaziz AA, Ishijima T, Seto T et al (2016) Characterization of surface dielectric barrier discharge influenced by intermediate frequency for ozone production. *Plasma Sources Sci Technol* 25:035012. <https://doi.org/10.1088/0963-0252/25/3/035012>
57. Zhang X, Lee BJ, Im HG, Cha MS (2016) Ozone production with dielectric barrier discharge: effects of power source and humidity. *IEEE Trans Plasma Sci* 44:2288–2296. <https://doi.org/10.1109/TPS.2016.2601246>
58. Pekárek S, Mikeš J (2014) Temperature-and airflow-related effects of ozone production by surface dielectric barrier discharge in air. *Eur Phys J D* 68:1–8. <https://doi.org/10.1140/epjd/e2014-50393-x>
59. Bataklijev T, Georgiev V, Anachkov M et al (2014) Ozone decomposition. *Interdiscip Toxicol* 7:47–59. <https://doi.org/10.2478/intox-2014-0008>
60. Kim HY, Kang SK, Kwon HC et al (2013) Gas temperature effect on reactive species generation from the atmospheric pressure air plasma. *Plasma Process Polym* 10:686–697. <https://doi.org/10.1002/ppap.201200163>
61. Jodzis S (2011) Application of technical kinetics for macroscopic analysis of ozone synthesis process. *Ind Eng Chem Res* 50:6053–6060. <https://doi.org/10.1021/ie102603z>
62. Benson SW, Axworthy AE (1957) Mechanism of the gas phase, thermal decomposition of ozone. *J Chem Phys* 26:1727–1733. <https://doi.org/10.1063/1.1743610>
63. Itoh H, Taguchi M, Suzuki S (2020) Thermal decomposition of ozone at high temperature leading to ozone zero phenomena. *J Phys D Appl Phys* 53:185206. <https://doi.org/10.1088/1361-6463/ab71a9>

64. Osawa N, Yoshioka Y (2015) Ozone and by-products generation characteristics by novel air-fed ozone generator which combines homogeneous discharge and filamentary discharge. In: 22th international symposium on plasma chemistry. Antwerp, Belgium, pp 5–9
65. Pavlovich MJ, Chang HW, Sakiyama Y et al (2013) Ozone correlates with antibacterial effects from indirect air dielectric barrier discharge treatment of water. *J Phys D Appl Phys* 46:145202. <https://doi.org/10.1088/0022-3727/46/14/145202>
66. Wang H, Zhuang Z, Sun Ch et al (2016) Numerical evaluation of the effectiveness of NO₂ and N₂O₃ generation during the NO ozonation process. *J Environ Sci (China)* 41:51–58. <https://doi.org/10.1016/j.jes.2015.05.015>
67. Abdelaziz AA, Ishijima T, Osawa N, Seto T (2019) Quantitative analysis of ozone and nitrogen oxides produced by a low power miniaturized surface dielectric barrier discharge: effect of oxygen content and humidity level. *Plasma Chem Plasma Process* 39:165–185. <https://doi.org/10.1007/s11090-018-9942-y>
68. Falkenstein Z, Coogan JJ (1997) Microdischarge behaviour in the silent discharge of nitrogen-oxygen and water-air mixtures. *J Phys D Appl Phys* 30:817–825. <https://doi.org/10.1088/0022-3727/30/5/015>
69. Ryzko H (1965) Drift velocity of electrons and ions in dry and humid air and in water vapour. *Proc Phys Soc* 85:1283–1295. <https://doi.org/10.1088/0370-1328/85/6/327>
70. Chen J, Wang P (2005) Effect of relative humidity on electron distribution and ozone production by DC coronas in air. *IEEE Trans Plasma Sci* 33:808–812. <https://doi.org/10.1109/TPS.2005.844530>
71. Lopez JL, Vezzu G, Freilich A, Paolini B (2013) Effects of hydrocarbon contamination on ozone generation with dielectric barrier discharges. *Eur Phys J D* 67:1–8. <https://doi.org/10.1140/epjd/e2013-40126-2>
72. Ono R, Oda T (2003) Dynamics of ozone and OH radicals generated by pulsed corona discharge in humid-air flow reactor measured by laser spectroscopy. *J Appl Phys* 93:5876–5882. <https://doi.org/10.1063/1.1567796>
73. Matsui K, Ikenaga N, Sakudo N (2015) Effects of humidity on sterilization of *Geobacillus stearothermophilus* spores with plasma-excited neutral gas. *Jpn J Appl Phys* 54:06GD02. <https://doi.org/10.7567/JJAP.54.06GD02>
74. de Baerdemaeker K, Nikiforov A, de Geyter N, Devlieghere F (2022) Cold plasma for bacterial decontamination: Impact of food matrix composition and RH of the input gas. In: 9th Central European symposium on plasma chemistry (CESPC-9) joint with COST action CA19110 Plasma Applications for Smart and Sustainable Agriculture (PIAagri). Faculty of Mathematics, Physics and Informatics, Comenius University in Bratislava, p 98

Publisher's Note Springer Nature remains neutral with regard to jurisdictional claims in published maps and institutional affiliations.